Integrated Difference Autocorrelation: A Novel Approach to Estimate Shear Wave Speed in the Presence of Compression Waves

Hamidreza Asemani, Jannick P. Rolland, and Kevin J. Parker

Abstract*—*Objective: **In shear wave elastography (SWE), the aim is to measure the velocity of shear waves, however unwanted compression waves and bulk tissue motion pose challenges in evaluating tissue stiffness. Conventional approaches often struggle to discriminate between shear and compression waves, leading to inaccurate shear wave speed (SWS) estimation. In this study, we propose a novel approach known as the integrated difference autocorrelation (IDA) estimator to accurately estimate reverberant SWS in the presence of compression waves and noise.** ***Methods:*** **The IDA estimator, unlike conventional techniques, computes the subtraction of velocity between neighboring particles, effectively minimizing the impact of long wavelength compression waves and other wide-area movements such as those caused by respiration. We evaluated the effectiveness of IDA by: (1) using k-Wave simulations of a branching cylinder in a soft background, (2) using ultrasound elastography on a breast phantom, (3) using ultrasound elastography in the human liver-kidney region, and (4) using magnetic resonance elastography (MRE) on a brain phantom.** ***Results:*** **By applying IDA to unfiltered contaminated wave fields of simulation and elastography experiments, the estimated SWSs are in good agreement with the ground truth values (i.e., less than 2% error for the simulation, 9% error for ultrasound elastography of the breast phantom and 19% error for MRE).** ***Conclusion:*** **Our results demonstrate that IDA accurately estimates SWS, revealing the existence of a lesion, even in the presence of strong compression waves.** ***Significance:*** **IDA exhibits consistency in SWS estimation across different modalities and excitation scenarios, highlighting its robustness and potential clinical utility.**

***Index Terms*—Integrated difference autocorrelation, magnetic resonance elastography, reverberant shear wave, shear wave elastography, ultrasound elastography.**

I. Introduction

SHEAR wave elastography (SWE) is an expanding imaging technique with applications in different modalities such as ultrasound [1], [2], [3], magnetic resonance imaging (MRI) [4], [5], and optical coherence tomography (OCT) [6], [7]. The capability of this method to estimate tissue stiffness and highlight different lesions positions it as a robust clinical tool for diagnosing a broad spectrum of diseases [8], [9], [10]. The fundamental concept of SWE remains consistent across different imaging modalities. Typically, shear waves are induced in the tissue through external excitation captured by the imaging modality and processed to compute the shear wave speed (SWS) map or tissue stiffness map [11], [12], [13], [14]. The resolution and accuracy of SWE are dependent on the imaging modality, the characteristics of the generated shear wave field, and the post-processing techniques applied [12], [15].

In SWE, the focus lies on measuring the speed of shear waves rather than compression waves, as unwanted compression waves and translational motions can introduce challenges in accurately assessing tissue stiffness. As illustrated in the classic text by Graff [16], a vibrating source on the surface of a body will impart shear waves, which are useful for elastography, but also significant compression waves and surface waves, which can confound the estimate of SWS. Compression waves and any other bulk tissue motion have long wavelengths (in the range of meters) and long correlation lengths compared to shear waves (with wavelengths in the range of a few millimeters), so they present an unwanted term if the analysis is oriented toward shear waves. Generally, these have been minimized by post-processing steps, including the calculation of the vector curl from 3D data or more simply from highpass filtering of 2D displacement data [17].

An example of filtering is given in [18], where Ormachea and Parker employed a 2D bandpass spatial filter to eliminate extremely low spatial frequency compressional waves and reduce high frequency noise in all directions. They used the cutoff spatial frequencies (f) related to the wavenumber k of the filter, which were set at $k_l = 2\pi f/C_{sh}$ and $k_h = 2\pi f/C_{sl}$, where C_{sl} and C_{sh} represented the chosen low and high SWSs,

Received 23 April 2024; revised 1 August 2024; accepted 14 September 2024. Date of publication 20 September 2024; date of current version 22 January 2025. This work was supported in part by the National Institutes of Health under Grant R21AG070331, and in part by the University of Rochester Center of Excellence in Data Science for Empire State Development under Grant 2089A015. *(Corresponding author: Hamidreza Asemani.)*

Hamidreza Asemani is with the Institute of Optics and Department of Electrical and Computer Engineering, University of Rochester, Rochester, NY 14642 USA (e-mail: hasemani@ur.rochester.edu).

Jannick P. Rolland is with the Institute of Optics and Department of Biomedical Engineering, University of Rochester, USA.

Kevin J. Parker is with the Department of Electrical and Computer Engineering and Department of Biomedical Engineering, University of Rochester, USA.

This article has supplementary downloadable material available at https://doi.org/10.1109/TBME.2024.3464104, provided by the authors.

Digital Object Identifier 10.1109/TBME.2024.3464104

respectively. Filtering contaminated wave fields is often challenging, especially when the range of SWS is not known *a priori*. Specifying the proper cutoffs for a 2D bandpass filter requires careful tuning in practice.

In this study, we introduce the difference autocorrelation estimator in order to calculate SWS in the presence of compression waves. By subtracting the velocity between two neighboring particles, we effectively minimize the impact of compression waves. This technique is capable of estimating SWS in fully reverberant shear wave fields, as well as imperfect or more directionally oriented shear wave fields. The application of the proposed approach is studied using (1) k-Wave elastography simulation of a stiff branching cylinder in a soft background, (2) ultrasound elastography of a breast phantom with a lesion (3) ultrasound elastography of the human liver kidney region, and (4) magnetic resonance elastography (MRE) of a brain phantom with two lesions.

II. Theory

The particle velocity $\boldsymbol{V}$ within a fully reverberant shear wave field is described as [19], [20] as

$$\boldsymbol{V}\ (\varepsilon, t) = \sum_{q,l} \hat{\boldsymbol{n}}_{ql}\ v_{ql}\ e^{i(k\hat{\boldsymbol{n}}_q \cdot\ \boldsymbol{\varepsilon} - \omega_0 t\ )}. \tag{1}$$

where $\boldsymbol{\varepsilon}$ signifies the position vector, t is time, ω_0 is the angular frequency, and the indices q and l correspond to realizations of the random unit vectors $\hat{\boldsymbol{n}}_{\boldsymbol{q}}$ and $\hat{\boldsymbol{n}}_{ql}$, respectively. The vector $\hat{\boldsymbol{n}}_q$ denotes the random direction of wave propagation, $\hat{\boldsymbol{n}}_{ql}$ indicates a random unit vector representing the direction of particle motion and v_{ql} represents an independent, identically distributed random variable signifying the magnitude of the particle velocity within a given realization. In transverse shear wave fields, the direction of wave propagation is orthogonal to the particle motion, indicating that $\hat{\boldsymbol{n}}_{ql}\ .\ \hat{\boldsymbol{n}}_q = 0$. However, the wave propagation and particle motion are in the same direction for compression waves, which implies $\hat{\boldsymbol{n}}_{ql}\ .\ \hat{\boldsymbol{n}}_q = 1$.

In the standard autocorrelation technique, the autocorrelation of the z-directed velocity field ($B_{V_zV_z}$) is conventionally computed in both space and time as described in [21] as

$$B_{V_zV_z}\ (\Delta\boldsymbol{\varepsilon},\ \Delta t) = E\left\{V_{\boldsymbol{z}}\left(\boldsymbol{\varepsilon}, t\right) V_{\boldsymbol{z}}{}^*\left(\boldsymbol{\varepsilon} + \Delta\boldsymbol{\varepsilon}, t + \Delta t\right)\right\} \tag{2}$$

where $\Delta\boldsymbol{\varepsilon}$ and Δt represent the small difference in position vector and time, respectively, E signifies an ensemble average, and the asterisk (*) indicates the complex conjugate. In practice, this equation takes the estimated particle velocities from an imaging system as a function of space and time. The presence of any unwanted compression waves in the tissue adds a long wavelength term to the autocorrelation equation. The estimated SWS in this condition is affected by the low spatial frequency compression waves. In order to overcome this issue and minimize the influence of compression waves and whole tissue motion, we propose to compute the autocorrelation of the quantity $V_{\boldsymbol{z}}(\boldsymbol{\varepsilon} - \Delta\boldsymbol{\varepsilon}) - \ V_{\boldsymbol{z}}(\boldsymbol{\varepsilon} + \Delta\boldsymbol{\varepsilon})$ instead of the autocorrelation of only the velocity field $V_{\boldsymbol{z}}$. The subtraction of particle velocities between neighboring particles effectively cancels out the contribution of compression waves with large wavelengths, leaving only the SWS component. Thus, the difference autocorrelation estimator $B_{DAV_zV_z}$ is defined, for simplicity when Δt is zero, as follows

$$\begin{aligned} &B_{DAV_zV_z}\ (\Delta\boldsymbol{\varepsilon}) \\ &\quad = E\ \{[V_z\left(\boldsymbol{\varepsilon} - \Delta\boldsymbol{\varepsilon}\right) - \ \ V_z\left(\boldsymbol{\varepsilon} + \Delta\boldsymbol{\varepsilon}\right)]\ \ [V_z\left(\boldsymbol{\varepsilon} - \Delta\boldsymbol{\varepsilon}\right) \\ &\qquad -V_z\left(\boldsymbol{\varepsilon} + \Delta\boldsymbol{\varepsilon}\right)]^*\} \\ &\quad = E\ \left\{\begin{array}{r} [V_{\boldsymbol{z}}\left(\boldsymbol{\varepsilon} - \Delta\boldsymbol{\varepsilon}\right)\ V_{\boldsymbol{z}}{}^*\left(\boldsymbol{\varepsilon} - \Delta\boldsymbol{\varepsilon}\right)] \\ +[V_{\boldsymbol{z}}\left(\boldsymbol{\varepsilon} + \Delta\boldsymbol{\varepsilon}\right)\ V_{\boldsymbol{z}}{}^*\left(\boldsymbol{\varepsilon} + \Delta\boldsymbol{\varepsilon}\right)] \\ -[V_{\boldsymbol{z}}\left(\boldsymbol{\varepsilon} - \Delta\boldsymbol{\varepsilon}\right)\ V_{\boldsymbol{z}}{}^*\left(\boldsymbol{\varepsilon} + \Delta\boldsymbol{\varepsilon}\right)] \\ -[V_{\boldsymbol{z}}\left(\boldsymbol{\varepsilon} + \Delta\boldsymbol{\varepsilon}\right)\ V_{\boldsymbol{z}}{}^*\left(\boldsymbol{\varepsilon} - \Delta\boldsymbol{\varepsilon}\right)] \end{array}\right\} \\ &\quad = 2\left(\overline{V_{\boldsymbol{z}}}^2\ - B_{V_zV_z}\left(2\Delta\boldsymbol{\varepsilon}\right)\right) \end{aligned} \tag{3}$$

where $\overline{V_{\boldsymbol{z}}}^2$ is the ensemble average velocity-squared and the simplified form is based on the fundamental definition of each of the terms, assuming spatially stationary statistics. Note also that any extra motion approximately constant across the autocorrelation window will be canceled by the subtraction in the first bracketed expressions.

In (3), $B_{V_zV_z}$ is the conventional spatial autocorrelation function. The autocorrelation function in different directions depends on the angle θ_s between the imaging system sensitivity (assumed to be z-directed) and the direction of $\Delta\boldsymbol{\varepsilon}$, defined by Aleman-Castañeda et al. [22] as follows

$$\begin{aligned} &B_{V_zV_z}\ (\Delta\boldsymbol{\varepsilon}, \Delta t) = \ 3\overline{V_{\boldsymbol{z}}}^2\ e^{i\omega_0\Delta t} \\ &\times\left\{\frac{\sin^2\theta_s}{2}\left[j_0\left(k\Delta\boldsymbol{\varepsilon}\right) - \frac{j_1\left(k\Delta\boldsymbol{\varepsilon}\right)}{k\Delta\boldsymbol{\varepsilon}}\right] + \ \cos^2\theta_s\ \frac{j_1\left(k\Delta\boldsymbol{\varepsilon}\right)}{k\Delta\boldsymbol{\varepsilon}}\right\}, \end{aligned} \tag{4}$$

where j_0 is the spherical Bessel function of the first kind of zero order and j_1 is the spherical Bessel function of the first kind of first order. In standard baseline autocorrelation estimation, $\Delta\boldsymbol{\varepsilon}$ is assumed to be aligned with one of the Cartesian axes. The angle θ_s in (4) is $\pi/2$ for $\Delta\varepsilon_x$ and $\Delta\varepsilon_y$, and zero for $\Delta\varepsilon_z$. Consequently, the standard baseline autocorrelation functions are defined as

$$B_{V_zV_z}\left(\Delta\varepsilon_x, \Delta t\right)\ = \frac{3}{2}\ \overline{V_{\boldsymbol{z}}}^2 e^{i\omega_0\Delta t}\ \left[j_0\left(k\Delta\varepsilon_x\right) - \frac{j_1\left(k\Delta\varepsilon_x\right)}{k\Delta\varepsilon_x}\right] \tag{5.a}$$

$$B_{V_zV_z}\left(\Delta\varepsilon_y, \Delta t\right)\ = \frac{3}{2}\overline{V_{\boldsymbol{z}}}^2 e^{i\omega_0\Delta t}\ \left[j_0\left(k\Delta\varepsilon_y\right) - \frac{j_1\left(k\Delta\varepsilon_y\right)}{k\Delta\varepsilon_y}\right] \tag{5.b}$$

$$B_{V_zV_z}\left(\Delta\varepsilon_z, \Delta t\right)\ = 3\overline{V_{\boldsymbol{z}}}^2 e^{i\omega_0\Delta t}\ \frac{j_1\left(k\Delta\varepsilon_z\right)}{k\Delta\varepsilon_z} \tag{5.c}$$

To enhance the robustness of the autocorrelation estimator, Asemani et al. [23], [24] introduced the angular integral autocorrelation (AIA) which involves computing the angular integral of the autocorrelation function within a two-dimensional plane spanning from 0 to 2π, resulting in the expression for the xz plane and yz plane as follows

$$B_{AIAxz}\ (\Delta\rho,\ \Delta t) = B_{AIAyz}\ \ (\Delta\rho,\ \Delta t)$$

$$= \frac{3}{4}\overline{V_z}^2 e^{i\omega_0 \Delta t}\left[j_0(k\Delta\rho) + \frac{j_1(k\Delta\rho)}{k\Delta\rho}\right] \quad (6)$$

where $\Delta\rho$ represents the one-dimensional lag in the autocorrelation argument subsequent to integration around θ_s. For the xy plane we have:

$$B_{AIAxy}(\Delta\rho, \Delta t) = \frac{3}{2}\overline{V_z}^2 e^{i\omega_0 \Delta t}\left[j_0(k\Delta\rho) - \frac{j_1(k\Delta\rho)}{k\Delta\rho}\right] \quad (7)$$

The difference autocorrelation for the standard baseline autocorrelation estimator can be obtained by assuming $\Delta t = 0$ and substituting (5) in (3) to yield

$$B_{DAz}(\Delta\varepsilon_x) = 2\left(\overline{V_z}^2 - \frac{3}{2}\overline{V_z}^2\left[j_0(2k\Delta\varepsilon_x) - \frac{j_1(2k\Delta\varepsilon_x)}{2k\Delta\varepsilon_x}\right]\right) \quad (8.a)$$

$$B_{DA_z}(\Delta\varepsilon_y) = 2\left(\overline{V_z}^2 - \frac{3}{2}\overline{V_z}^2\left[j_0(2k\Delta\varepsilon_y) - \frac{j_1(2k\Delta\varepsilon_y)}{2k\Delta\varepsilon_y}\right]\right) \quad (8.b)$$

$$B_{DA_z}(\Delta\varepsilon_z) = 2\left(\overline{V_z}^2 - 3\overline{V_z}^2 e^{i\omega_0 \Delta t}\frac{j_1(2k\Delta\varepsilon_z)}{2k\Delta\varepsilon_z}\right) \quad (8.c)$$

By substituting (6) or (7) in (3), the integrated difference autocorrelation (IDA) for different autocorrelation planes can be obtained as

$$B_{IDAxz}(\Delta\rho) = B_{IDA\,yz}(\Delta\rho) = 2\left(\overline{V_z}^2 - \frac{3}{4}\overline{V_z}^2\left[j_0(2k\Delta\rho) + \frac{j_1(2k\Delta\rho)}{2k\Delta\rho}\right]\right) \quad (9)$$

$$B_{IDAxy}(\Delta\rho) = 2\left(\overline{V_z}^2 - \frac{3}{2}\overline{V_z}^2\left[j_0(2k\Delta\rho) - \frac{j_1(2k\Delta\rho)}{2k\Delta\rho}\right]\right) \quad (10)$$

Fig. 1(a) displays the autocorrelation curves for the z-directed simple autocorrelation functions and the AIA function in the xz plane. The magnitude of the small difference in position ($\Delta\varepsilon_x$, $\Delta\varepsilon_z$, and $\Delta\rho$) ranges from zero to one pixel less than the size of the autocorrelation window. As depicted in this figure, the curves for the autocorrelation functions ($B_{V_zV_z}(\Delta\varepsilon_x)$ and $B_{V_zV_z}(\Delta\varepsilon_z)$) are distinct, and the AIA function is consistently positioned between them. The maximum occurs at zero lag for all autocorrelation functions. Fig. 1(b) presents z-directed difference autocorrelation curves of $\Delta\varepsilon_x$ and $\Delta\varepsilon_z$, along with the IDA curve in the xz plane. The IDA curve consistently falls between the simple difference autocorrelation curves. At zero lag, the value for the difference autocorrelation functions is zero. In practice, a curve fit of measured data to (9), (10) is necessary. Fig. 1(b) is utilized to derive a best fit estimate of wavenumber k, thereby determining SWS from the physics definition $k = \omega/C_s$ and where ω is the applied radial frequency and C_s is taken in this context as equal to the SWS.

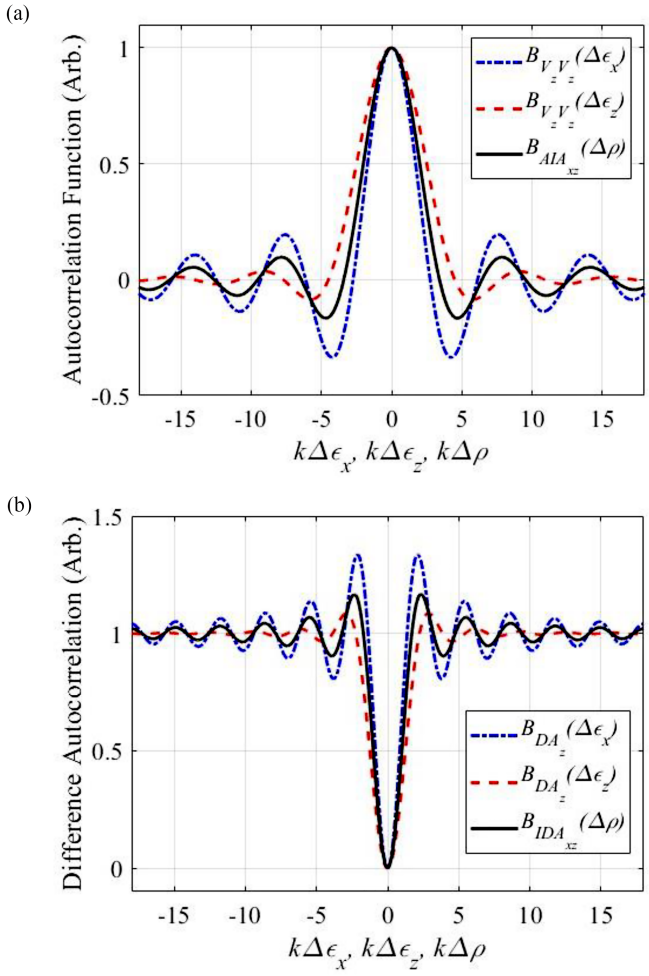

Fig. 1. Autocorrelation and difference autocorrelation curves: (a) Curves for the z-directed simple autocorrelation functions and the AIA function in the xz plane, (b) curves for z-directed difference autocorrelation functions of $\Delta\varepsilon_x$ and $\Delta\varepsilon_z$, along with the IDA function in the xz plane.

III. k-Wave Elastography Simulation

The effectiveness of the proposed IDA approach was evaluated using the k-Wave simulation toolbox in MATLAB (The MathWorks, Inc. Natick, MA, USA, version 2022b) [25] of a stiff branching cylinder in a soft background. Both the background medium and the y-shaped inclusion were modeled as uniform isotropic materials, with SWS of 1 m/s and 2 m/s, respectively. The simulation geometry and the defined SWS properties for the y-shaped cylinder and the background are presented in Fig. 2(a). Further details regarding this simulation can be found in [23]. A fully reverberant shear wave field at a frequency of 200 Hz was created by the application of multiple shear wave point sources around the outer boundary. A white Gaussian noise with a signal-to-noise ratio (SNR) of 10 dB was added to the shear wave field. The resulting shear wave field was purposely superimposed with compression waves, modeled as a long wavelength phasor of the same temporal frequency and approximately the same amplitude. It is assumed that the transducer was positioned on the top side of the model and the velocity field was specifically measured along the z-axis to mimic realistic scanning conditions in elastography. Fig. 2(b) presents an unfiltered phase map of the wave field at 200 Hz, revealing the reverberant shear wave field superimposed onto a longer spatial scale of compression waves.

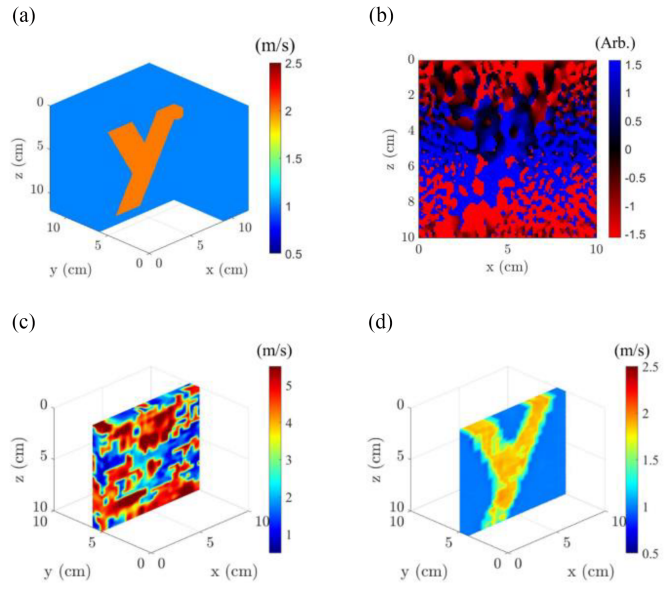

Fig. 2. k-Wave elastography simulation: (a) Simulation geometry and defined SWS properties for the y-shaped inclusion and the background, (b) unfiltered phase map of the contaminated wave field at the excitation frequency of 200 Hz, demonstrating both small scale shear wave patterns and larger scale compression wave pattern, (c) SWS map estimated by applying AIA to the unfiltered contaminated wave field, (d) SWS map estimated by applying IDA to the unfiltered contaminated wave field.

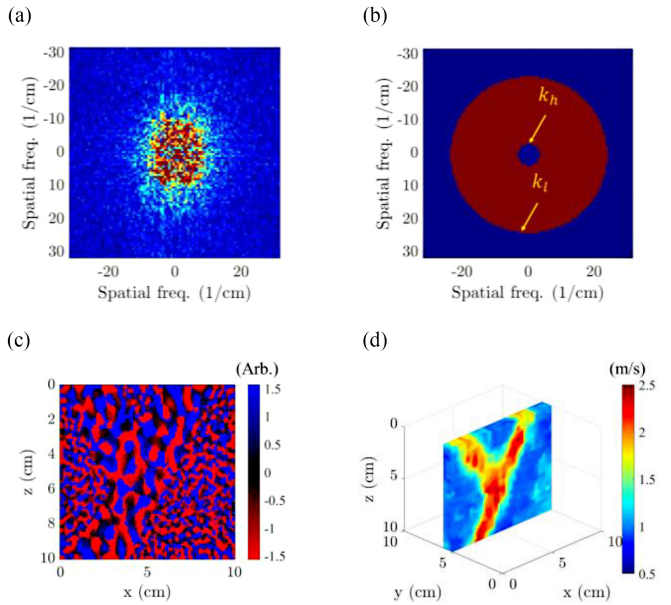

Fig. 3. Process of 2D bandpass filtering and SWS estimation using AIA in k-Wave simulation: (a) Magnitude of the 2D spatial Fourier transform of the k-Wave displacement field at the excitation frequency of 200 Hz, (b) 2D bandpass filter in the Fourier domain used to eliminate compression waves, (c) phase map of the shear wave field after 2D bandpass filtering at the frequency of 200 Hz, (d) SWS map estimated by applying AIA to the filtered phase map of the shear wave field at the frequency of 200 Hz.

The animated sequence of the shear wave field is available in the supplementary materials.

A square autocorrelation window 15 mm in size was utilized in all simulation measurements to estimate the SWS. A central 3D region of interest was selected to reduce the memory and computational costs. The SWS map estimated by applying the AIA to the unfiltered contaminated wave field is illustrated in Fig. 2(c). Due to the presence of compression waves in the shear wave field, SWS estimation using conventional methods is challenging, and the y-shaped inclusion is not discernible against the background. The average SWS in the background was estimated to be 3.41 m/s (i.e., 241% error). Fig. 2(d) displays the SWS map estimated by applying the IDA to the unfiltered contaminated wave field, where the y-shaped inclusion is clearly highlighted. The average SWS in the background was estimated to be 0.98 m/s (i.e., 2% error)

Although AIA fails in estimating SWS when applied to contaminated wave fields, effective filtering techniques can enhance its efficiency and accuracy. In Fig. 3(a), the magnitude of the 2D spatial Fourier transform of the k-Wave displacement field at 200 Hz is depicted. The central red zone signifies the presence of high-energy, low spatial frequency waves or compression waves within the wave field.

A 2D bandpass filter was determined based on a maximum value for the SWS (corresponding to minimum value for wavenumber k), and a minimum value for the SWS (corresponding to maximum value for wavenumber k), according to $C_s = 2\pi f/k$. Following numerous trials using different lower and upper values, the optimal values were determined, with the lower value designated as $C_{sl} = 0.54$ m/s and the upper value as $C_{sh} = 3.89$ m/s. Considering a frequency of 200 Hz, these values correspond to $k_l = 23.26$ cm^{-1} and $k_h = 3.23$ cm^{-1}. Fig. 3(b) displays the 2D bandpass filter defined for k-Wave elastography, presenting lower wavenumber k_l and upper wavenumber k_h values. Fig. 3(c) depicts the phase map of the shear wave field at 200 Hz after applying a 2D bandpass filtering. In this case with perfect *a priori* information, the compression waves are eliminated and a fully reverberant shear wave field is obtained. Employing AIA on the filtered phase map of Fig. 3(c) led to the estimation of the SWS map, presented in Fig. 3(d). The average SWS in the background was estimated to be 0.98 m/s (i.e., 2% error).

IV. Ultrasound Elastography of Breast Phantom

In order to explore the effectiveness of the difference autocorrelation method, a dataset of ultrasound elastography experiments on a CIRS breast phantom (model 509, CIRS Inc., Norfolk, Virginia, USA) was utilized. The CIRS breast phantom mimics the breast tissue characteristics and contains several lesions of different sizes. A Verasonics ultrasound system (V-1, Verasonics Inc., Kirkland, WA, USA) connected to a linear array ultrasound transducer (Model L7-4, ATL, Bothell, WA, USA) with a 5 MHz center frequency was utilized in this experiment. The sampling frequency was 20 MHz. Four mechanical vibration sources were used in the elastography experiment to generate a reverberant shear wave field. A 3D matrix of in-phase and quadrature (IQ) data was collected for postprocessing. To calculate the axial particle displacements, a Loupas estimator [26] was employed. The dataset contains the displacement fields

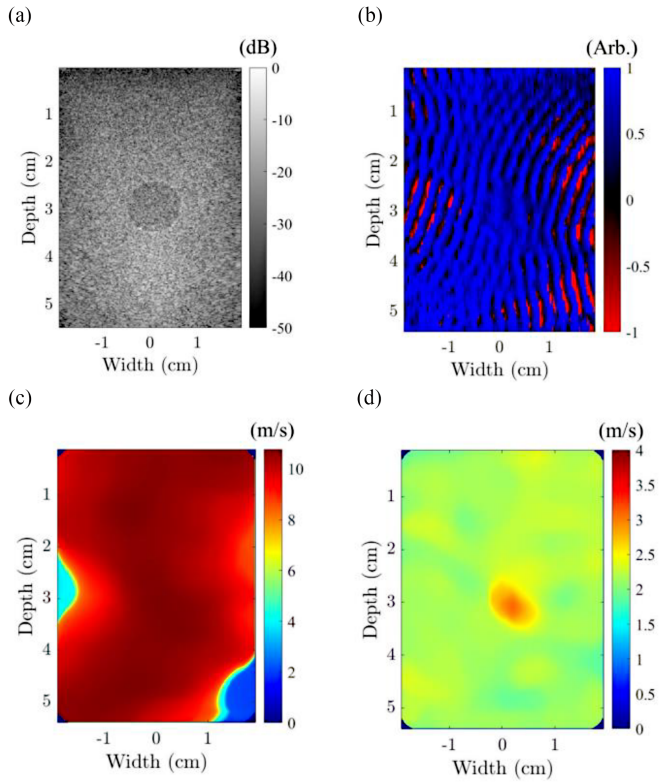

Fig. 4. Ultrasound elastography of a breast phantom with a lesion: (a) B-mode ultrasound scan of the phantom, (b) unfiltered phase map of the contaminated wave field at the excitation frequency of 900 Hz, (c) SWS map estimated by applying AIA to the unfiltered contaminated wave field, (d) SWS map estimated by applying IDA to the unfiltered contaminated wave field.

of reverberant shear wave fields at three different excitation frequencies including 900 Hz, 600 Hz, and 400 Hz. Detailed descriptions of the experiments can be found in [18] and [23].

Fig. 4(a) displays the B-mode ultrasound scan of the breast phantom revealing the presence of a lesion. Fig. 4(b) presents the unfiltered phase map of the wave field at an excitation frequency of 900 Hz and the short-wavelength reverberant shear wave field is superimposed with a long-wavelength (low spatial frequency) compression wave. The motion movie of the shear wave field is available in the supplementary materials. Fig. 4(c) displays a SWS map estimated by applying AIA to the unfiltered contaminated wave field. A 7.5 mm square autocorrelation window was used for all breast phantom ultrasound elastography measurements.

Applying the IDA to the unfiltered contaminated wave field of Fig. 4(b) yields the SWS map depicted in Fig. 4(d). The lesion in the SWS map is effectively highlighted against the uniform background in Fig. 4(d), and the average SWS using IDA was estimated to be 2.09 m/s in the background at 900 Hz. Similarly, the IDA approach was applied to the elastography displacement field at excitation frequencies of 600 Hz and 400 Hz, and consistent outcomes were obtained (see Table I). The average SWS in the background using IDA was determined to be 2.07 m/s at 600 Hz and 2.10 m/s at 400 Hz. Ormachea and Parker [18] reported an average SWS of 2.27 m/s in various frequencies including 900 Hz, 600 Hz, and 400 Hz, while Asemani et al. [23] reported a slightly lower value of 2.26 m/s.

TABLE I
SWS IN THE BACKGROUND ESTIMATED BY APPLYING AIA AND IDA APPROACHES TO UNFILTERED CONTAMINATED WAVE FIELDS OF THE BREAST PHANTOM ULTRASOUND ELASTOGRAPHY ACROSS DIFFERENT EXCITATION FREQUENCIES

Excitation frequency	SWS (m/s) in breast phantom using AIA	Estimation error using AIA	SWS (m/s) in breast phantom using IDA	Estimation error using IDA
900 Hz	9.80 ± 1.73	332%	2.09 ± 0.11	8%
600 Hz	1.74 ± 0.09	23%	2.07 ± 0.09	9%
400 Hz	1.65 ± 0.10	27%	2.10 ± 0.10	7%

In contrast, while AIA proves to be a robust approach for estimating SWS in the presence of noise and reverberance [23], it fails to accurately estimate SWS in a shear wave field superimposed with compression waves. As depicted in Fig. 4(d), AIA yielded significantly higher SWS estimates due to the presence of low spatial frequency and long wavelength compression waves. The average SWS in the background using AIA was estimated to be 9.80 m/s at 900 Hz which is far from the ground truth value. Furthermore, the lesion is not visible in the SWS map estimated using AIA. Table I compares the SWS in the background, estimated using the AIA and IDA approaches on the unfiltered contaminated wave fields across different excitation frequencies.

Fig. 5(a) shows the magnitude of the 2D spatial Fourier transform of the breast phantom displacement field at 900 Hz. The red zone at the center indicates that there are high energy, low spatial frequency waves or compression waves in the wave field. Fig. 5(b) presents the 2D bandpass filter with specified lower and upper values. After several iterations to determine the optimal lower and upper values for the frequency of 900 Hz, the lower value was set to $C_{sl} = 0.30$ m/s and the upper value was set to $C_{sh} = 6.79$ m/s which correspond to $k_l = 188.50$ cm^{-1} and $k_h = 8.33$ cm^{-1} (see Fig. 5(b)). The phase map of the displacement field after the 2D bandpass filtering at 900 Hz is displayed in Fig. 5(c). Applying AIA to the filtered phase map of Fig. 5(c) resulted in the estimated SWS map shown in Fig. 5(d). The lesion is highlighted in the SWS map with the average SWS in the background estimated to be 2.45 m/s (i.e., 8% error).

V. ULTRASOUND ELASTOGRAPHY OF LIVER-KIDNEY

In this section, the effectiveness of the developed IDA estimator is explored using a dataset of ultrasound elastography focusing on the human liver-kidney region. The dataset contains B-mode ultrasound scans and displacement field data captured from fully reverberant shear waves across a diverse spectrum of excitation frequencies, including 702 Hz, 585 Hz, 468 Hz, 351 Hz, 234 Hz, and 117 Hz. This ultrasound elastography experiment was performed under the requirements of informed consent of the South-woods Imaging Clinical Institutional Review Board.

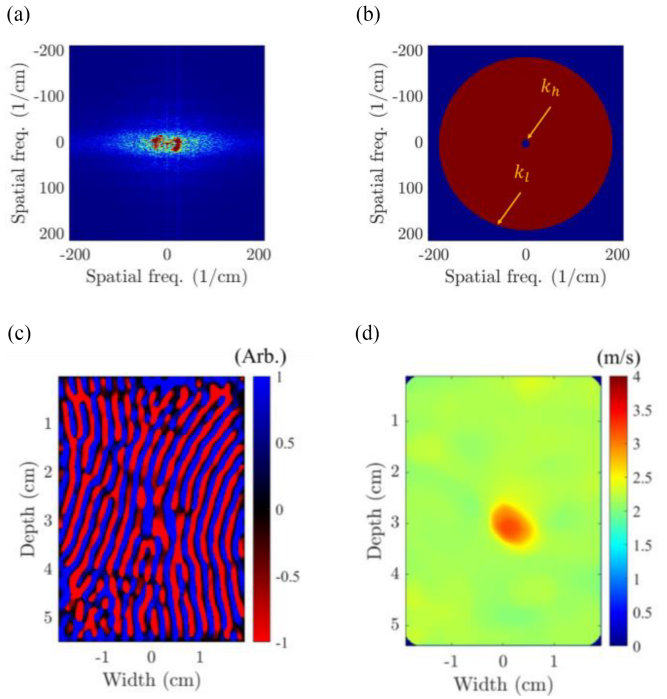

Fig. 5. Process of 2D bandpass filtering and SWS estimation in breast phantom ultrasound elastography dataset: (a) Magnitude of the 2D spatial Fourier transform of displacement field at the frequency of 900 Hz, (b) 2D bandpass filter in the Fourier domain used to eliminate compression waves, (c) phase map of the shear wave field after 2D bandpass filtering at the frequency of 900 Hz, (d) SWS map estimated by applying AIA on the filtered phase map of the shear wave field at the frequency of 900 Hz.

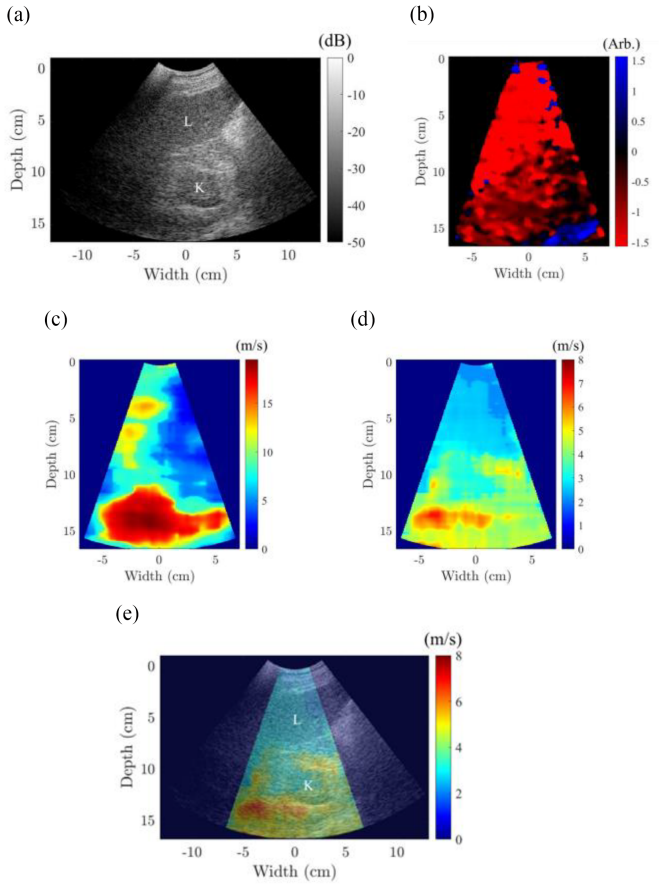

Fig. 6. Ultrasound elastography of a human liver-kidney region: (a) B-mode ultrasound scan of the liver-kidney, (b) unfiltered phase map of the contaminated wave field at the excitation frequency of 702 Hz, (c) SWS map estimated by applying AIA to the unfiltered contaminated wave field, (d) SWS map estimated by applying IDA to the unfiltered contaminated wave field, (e) estimated SWS map obtained from the IDA overlaid on the B-mode ultrasound scan of the liver-kidney region.

A Verasonics ultrasound system (Vantage-128$^{\text{TM}}$, Verasonics Inc., Kirkland, WA, USA) with a 3 MHz center frequency, connected to a convex ultrasound probe (model C4-2, ATL, Bothell, WA, USA) was utilized. To track the induced displacements, a Loupas estimator [26] was employed. The sampling frequency was set to 12 MHz and the tracking pulse repetition frequency (PRF) was set to 3600 Hz with a total acquisition time of 0.5 s. A custom-made portable trifold futon with eight electromagnetic vibration drivers (Quad Resonator Model EI718$^{\text{TM}}$, Elastance Imaging LLC, Columbus, OH, USA) was used to induce the reverberant shear wave field into the body surrounding the liver and kidney. These drivers were positioned within a square configuration. Further details regarding the *in vivo* experiment can be found in [23] and [27].

The B-mode ultrasound scan of an anatomical view of the liver and kidney is illustrated in Fig. 6(a). The scan reveals both tissues, the liver (zone L) depicted by distinct darker zones, and the kidney (zone K) depicted by a rounded region. Fig. 6(b) represents the unfiltered phase map of the liver-kidney wave field at an excitation frequency of 702 Hz, showcasing the reverberant shear wave field superimposed with the low spatial frequency compression waves. The motion movie of the shear wave field, available in the supplementary materials, highlights the effect of compression waves on the shear wave field. All measurements in ultrasound elastography of the liver-kidney region utilized a square autocorrelation window 18.5 mm in size.

Fig. 6(c) presents the SWS map estimated using AIA on the unfiltered contaminated wave field at a frequency of 702 Hz. The liver and kidney regions are not discernible in this SWS map, and the average SWS in the liver and kidney were estimated to be 9.32 m/s and 7.14 m/s, respectively. Fig. 6(d) displays the SWS map estimated using IDA on the unfiltered contaminated wave field of liver-kidney. The average SWS was estimated to be 2.57 m/s in the liver and 3.65 m/s in the kidney. The regions for measuring the average SWS are indicated by two dashed rectangles in Fig. 6(d). Fig. 6(e) showcases the estimated SWS map obtained from the IDA overlaid on the B-mode ultrasound scan of the liver-kidney region. Both the liver region and the kidney region are visualized in the IDA SWS map.

Asemani et al. [23] reported average SWS values of 2.69 m/s in the liver and 3.98 m/s in the kidney. As expected, unlike IDA, the AIA approach fails to accurately estimate SWS in ultrasound elastography of the liver-kidney when the shear wave field is superimposed with compression waves. The IDA estimator was applied to the unfiltered wave field at other excitation frequencies, including 585 Hz, 468 Hz, 351 Hz, 234 Hz, and 117 Hz, yielding consistent results (see Table II). Table II presents a

TABLE II
SWS IN THE LIVER AND THE KIDNEY ESTIMATED BY APPLYING AIA AND IDA APPROACHES TO UNFILTERED CONTAMINATED WAVE FIELDS OF LIVER-KIDNEY ULTRASOUND ELASTOGRAPHY ACROSS DIFFERENT EXCITATION FREQUENCIES

Excitation frequency	SWS (m/s) in liver using AIA	SWS (m/s) in liver using IDA	SWS (m/s) in kidney using AIA	SWS (m/s) in kidney using IDA	SWS ratio using AIA	SWS ratio using IDA
702 Hz	9.32 ± 2.33	2.57 ± 0.04	7.14 ± 1.98	3.65 ± 0.39	0.77 ± 0.29	1.42 ± 0.15
585 Hz	7.41 ± 1.84	2.20 ± 0.13	15.11 ± 0.44	3.31 ± 0.12	2.04 ± 0.51	1.50 ± 0.10
468 Hz	1.85 ± 0.18	1.78 ± 0.34	11.04 ± 0.57	2.72 ± 0.07	5.97 ± 0.66	1.53 ± 0.29
351 Hz	6.08 ± 2.42	1.21 ± 0.10	9.06 ± 0.16	1.74 ± 0.25	1.49 ± 0.59	1.44 ± 0.24
234 Hz	6.38 ± 0.20	0.78 ± 0.08	6.90 ± 0.02	1.23 ± 0.10	1.08 ± 0.03	1.58 ± 0.21
117 Hz	1.58 ± 0.18	0.41 ± 0.03	3.45 ± 0.03	0.65 ± 0.11	2.18 ± 0.25	1.59 ± 0.29

comparison of SWS in the liver and the kidney, estimated using AIA and IDA approaches on the unfiltered contaminated wave fields across different excitation frequencies.

Fig. 7(a) depicts the magnitude of the 2D spatial Fourier transform of the liver-kidney displacement field at the frequency of 702 Hz. The red region in the center indicates the presence of compression waves in the wave field. The lower value for the 2D bandpass filter was set to $C_{sl} = 1.30$ m/s and the upper value was set to $C_{sh} = 7$ m/s which correspond to $k_l = 33.93$ cm^{-1} and $k_h = 6.30$ cm^{-1}. The 2D bandpass filter used to eliminate compression waves is presented in Fig. 7(b), and the phase map of the displacement field after the 2D bandpass filtering is shown in Fig. 7(c). Fig. 7(d) illustrates the SWS map estimated using AIA on the filtered displacement field. The liver and kidney regions are highlighted in the SWS map and the average SWS is estimated to be 2.69 m/s in the liver and 3.98 m/s in the kidney.

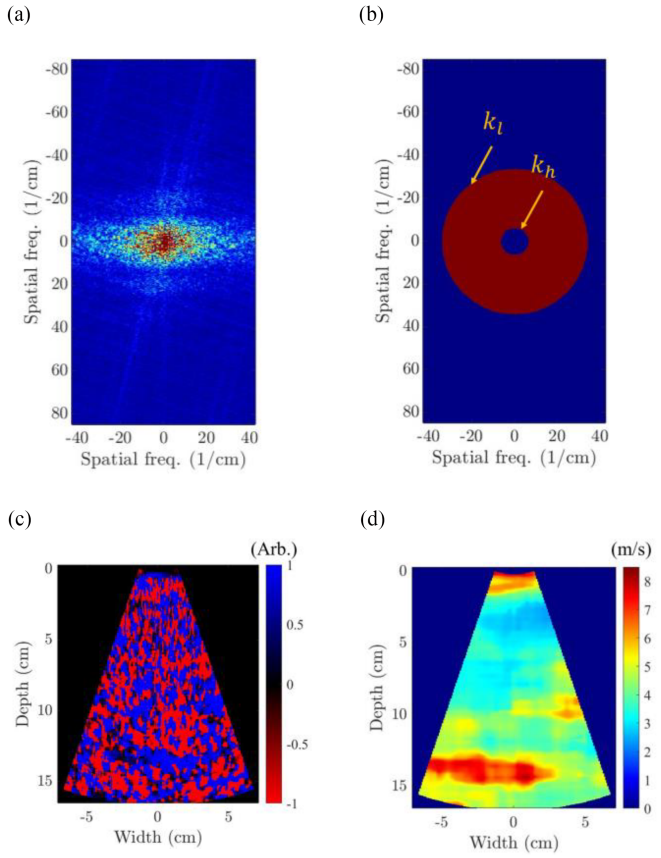

Fig. 7. Process of 2D bandpass filtering and SWS estimation in liver-kidney ultrasound elastography dataset: (a) Magnitude of the 2D spatial Fourier transform of the displacement field at the excitation frequency of 702 Hz, (b) 2D bandpass filter in the Fourier domain used to eliminate compression waves, (c) phase map of the shear wave field after 2D bandpass filtering at the frequency of 702 Hz, (d) SWS map estimated by applying AIA to the filtered phase map of the shear wave field at the frequency of 702 Hz.

VI. MAGNETIC RESONANCE ELASTOGRAPHY OF BRAIN PHANTOM

In order to assess the effectiveness of the developed IDA approach across different modalities and excitation scenarios, the performance of this approach was evaluated using an MRE dataset of a brain phantom containing two lesions. A whole-body 3T MRI scanner (Prisma, Siemens, Erlangen, Germany) equipped with a 20-channel head coil was used for all MRE experiments. The single-shot echo-planar imaging (EPI) sequence was implemented to capture the time-varying harmonic tissue displacements. The MR scanner settings included an echo time of 76.0 ms and a repetition time of 8640 ms. Forty axial slices with an isotropic voxel size of 1.6 mm were acquired for the phantom. A pneumatic mechanical actuator was used to generate the reverberant shear wave field within the phantom. The actuator was placed at the bottom of the brain phantom and was configured to move in the vertical (depth) direction. The details of the experiments can be found in [28].

Fig. 8(a) presents a B-mode MRI scan of a cross-section in the *xy* plane of the brain phantom. The brain phantom included two spherical gelatin lesions, with diameters of 18 mm and 12 mm, respectively. The unfiltered phase map of the Y-motion wave field at an excitation frequency of 200 Hz is illustrated in Fig. 8(b). The motion movie for the wave field is provided in the supplementary materials. The Y-motion demonstrates superimposition with large wavelength and low spatial frequency compression waves, rendering the shear wave pattern indiscernible. In Kabir et al. [28], the background shear modulus for the brain phantom is reported as 3.34 ± 0.04 kPa, which corresponds to SWS of 1.83 m/s. Fig. 8(c) shows the SWS map estimated by applying AIA to the Y-motion displacement field. The average SWS in the background using AIA on the unfiltered wave field is estimated to be 4.89 m/s. Lesions are not visualized in the SWS map and the AIA approach fails to estimate SWS in the unfiltered contaminated wave field of Y-motion, as expected.

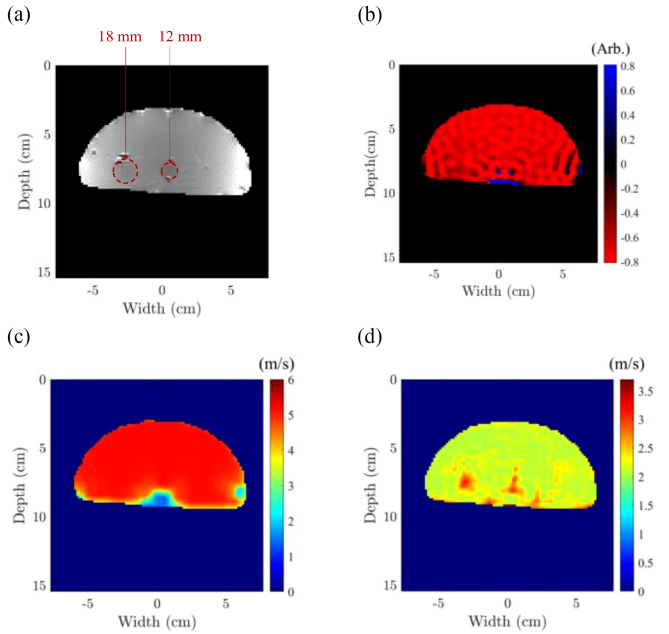

Fig. 8. MRE of a brain phantom with one 18 mm diameter lesion and one 12 mm diameter lesion at the excitation frequency of 200 Hz: (a) B-mode MRI scan of the phantom (lesion locations and sizes are highlighted by dashed circles), (b) unfiltered phase map of the contaminated wave field of Y-motion, (c) SWS map estimated by applying AIA to the unfiltered contaminated wave field of Y-motion, (d) SWS map estimated by applying IDA to the unfiltered contaminated wave field of Y-motion.

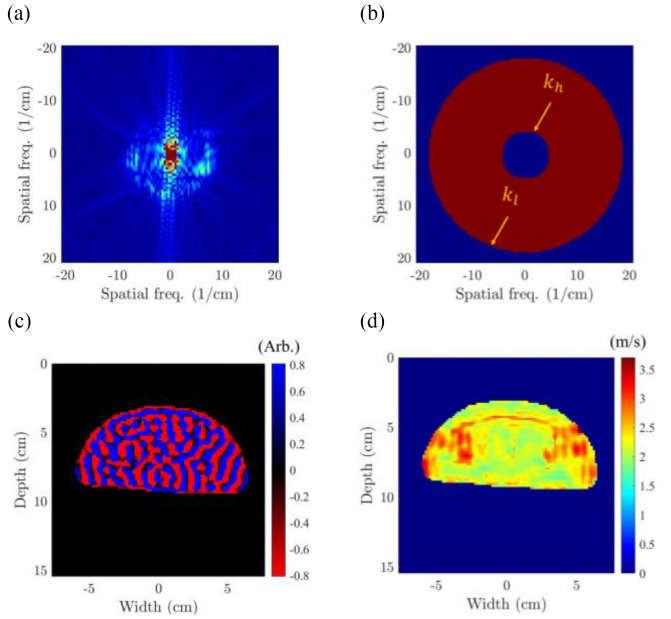

Fig. 9. Process of 2D bandpass filtering and SWS estimation using AIA in MRE dataset: (a) Magnitude of the 2D spatial Fourier domain of Y-motion displacement field at the excitation frequency of 200 Hz, (b) 2D bandpass filter in the Fourier domain used to eliminate compression waves, (c) phase map of the Y-motion shear wave field after 2D bandpass filtering at the frequency of 200 Hz, (d) SWS map estimated by applying AIA to the filtered shear wave field of Y-motion at the frequency of 200 Hz.

Fig. 8(d) depicts the SWS map estimated by applying the IDA estimator to the unfiltered contaminated wave field of Y-motion at the frequency of 200 Hz. A 10.7 mm square autocorrelation window was applied in all MRE measurements. Lesions are successfully highlighted in this SWS map, and the average background SWS is estimated to be 2.18 m/s (i.e., 19% error). The MRE result demonstrates the IDA's effectiveness in estimating SWS in the highly contaminated wave field, without requiring any filtering. This validates the robustness of the IDA estimator in the presence of compression waves.

As discussed in Section III, the effectiveness of the AIA approach in the presence of compression waves may be enhanced when used alongside appropriate filtering techniques. Fig. 9 illustrates the filtering process in the MRE dataset. In Fig. 9(a), the magnitude of the 2D spatial Fourier domain of the MRE displacement field at a frequency of 200 Hz is presented. The prominent red zone in the center indicates the presence of strong low spatial frequency waves or compression waves contaminating the shear wave field. This extensive red zone signifies the strength and wide spatial frequency range of the compression waves.

Fig. 9(b) showcases the 2D bandpass filter tailored for the MRE dataset in the Fourier domain. After experimenting with different combinations of lower and upper values, optimal results were achieved with the lower value set to $C_{sl} = 0.68$ m/s and the upper value set to $C_{sh} = 2.80$ m/s which corresponds to $k_l = 18.48$ cm^{-1} and $k_h = 4.49$ cm^{-1}. Fig. 9(c) displays the phase map of the shear wave field after 2D bandpass filtering at the frequency of 200 Hz. The impact of the compression wave is notably reduced, and the reverberant shear wave pattern becomes discernible. The motion movie of the shear wave field after filtering is provided in the supplementary materials.

Fig. 9(d) exhibits the estimated SWS map using AIA on a filtered shear wave field of Y-motion at the frequency of 200 Hz. The average SWS in the background estimated using AIA is 2.30 m/s (i.e., 26% error), and the lesions are not visualized in this SWS map. This illustrates that even after filtering and mitigating the effects of compression waves, AIA may fail in visualizing lesions and estimating SWS, particularly when the shear wave field is superimposed with compression waves exhibiting a wide spatial frequency range. In contrast, IDA consistently proves effective in SWS estimation, even in the presence of strong compression waves across a wide spatial frequency range.

VII. Conclusion

This study describes the novel IDA estimator for SWS estimation in the presence of compression waves. Through comprehensive evaluations using k-Wave simulations and experimental data from ultrasound elastography and MRE, we have demonstrated the effectiveness and robustness of IDA in accurately estimating SWS across various tissue types and imaging modalities where the presence of long wavelength compression waves complicates the calculation of shear wave properties. There are several advantages to the newer IDA approach. There is no need to have 3D vector data to implement the vector curl operator.

Further, careful *a priori* estimates of wavelengths to fine tune a bandpass filter are not required. The IDA is estimated directly from the velocity data using the autocorrelation operation in 2D, integrated to a one-dimensional (radial average) function of lag. In a k-Wave model of a stiff y-shaped cylinder within a uniform soft background, the IDA estimator displayed advanced capabilities in highlighting the y-shaped inclusion and estimating the SWS in the background accurately with a 2% error. In ultrasound elastography of a breast phantom with a lesion, IDA effectively highlighted the lesion and consistently estimated SWS values across different excitation frequencies with less than 9% error, demonstrating its reliability in complex wave fields with imperfect reverberation and compression waves. Similarly, in ultrasound elastography of the liver-kidney region, IDA successfully visualized liver and kidney tissues, providing consistent SWS estimates, even in the presence of compression wave contamination, thus establishing its effectiveness in clinical scenarios. In the MRE of a brain phantom with two lesions, IDA showcased its capability to reasonably estimate SWS with a 19% error effectively highlighting lesions even in a highly contaminated wave field. The comprehensive evaluation across multiple modalities and excitation scenarios in this study underscores the robustness and potential clinical applicability of the IDA approach in shear wave elastography.

Acknowledgment

The authors are grateful to Elastance Imaging, Inc. and Dr. Richard Barr for sharing a scan from their previous studies.

References

[1] J. M. Cormack et al., "Focused shear wave beam propagation in tissue-mimicking phantoms," *IEEE Trans. Biomed. Eng.*, vol. 71, no. 2, pp. 621–630, Feb. 2024, doi: 10.1109/TBME.2023.3311688.

[2] J. Ormachea et al., "Shear wave speed estimation using reverberant shear wave fields: Implementation and feasibility studies," *Ultrasound Med. Biol.*, vol. 44, no. 5, pp. 963–977, May 2018, doi: 10.1016/j.ultrasmedbio.2018.01.011.

[3] S. Hirsch et al., "Compression-sensitive magnetic resonance elastography," *Phys. Med. Biol.*, vol. 58, no. 15, pp. 5287–5299, Aug. 2013, doi: 10.1088/0031-9155/58/15/5287.

[4] H. Herthum et al., "Multiple motion encoding in phase-contrast MRI: A general theory and application to elastography imaging," *Med. Image Anal.*, vol. 78, no. 1, May 2022, Art. no. 102416, doi: 10.1016/j.media.2022.102416.

[5] I. Sack, "Magnetic resonance elastography from fundamental soft-tissue mechanics to diagnostic imaging," *Nat. Rev. Phys.*, vol. 5, no. 1, pp. 25–42, Jan. 2023, doi: 10.1038/s42254-022-00543-2.

[6] F. Zvietcovich and K. V. Larin, "Wave-based optical coherence elastography: The 10-year perspective," *Prog. Biomed. Eng.*, vol. 4, no. 1, Jan. 2022, Art. no. 012007, doi: 10.1088/2516-1091/ac4512.

[7] F. Zhang et al., "Quantitative optical coherence elastography of the optic nerve head in vivo," *IEEE Trans. Biomed. Eng.*, vol. 71, no. 3, pp. 732–737, Mar. 2024, doi: 10.1109/TBME.2023.3316606.

[8] S. S. Poul and K. J. Parker, "Fat and fibrosis as confounding cofactors in viscoelastic measurements of the liver," *Phys. Med. Biol.*, vol. 66, no. 66, Feb. 2022, Art. no. 045024, doi: 10.1088/1361-6560/abd593.

[9] G. R. Ge et al., "Theory of sleep/wake cycles affecting brain elastography," *Phys. Med. Biol.*, vol. 67, no. 22, Nov. 2022, Art. no. 225013, doi: 10.1088/1361-6560/ac9e40.

[10] A. Manduca et al., "MR elastography: Principles, guidelines, and terminology," *Magn. Reason. Med.*, vol. 85, no. 5, pp. 2377–2390, May 2021, doi: 10.1002/mrm.28627.

[11] R. M. S. Sigrist et al., "Ultrasound elastography: Review of techniques and clinical applications," *Theranostics*, vol. 7, no. 5, pp. 1303–1329, Mar. 2017, doi: 10.7150/thno.18650.

[12] Y. K. Mariappan et al., "Magnetic resonance elastography: A review," *Clin. Anat.*, vol. 23, no. 5, pp. 497–511, Jul. 2010, doi: 10.1002/ca.21006.

[13] B. F. Kennedy et al., "A review of optical coherence elastography: Fundamentals, techniques and prospects," *IEEE J. Sel. Top. Quantum Electron.*, vol. 20, no. 2, Mar./Apr. 2014, Art. no. 7101217, doi: 10.1109/JSTQE.2013.2291445.

[14] J.-L. Gennisson et al., "Ultrasound elastography: Principles and techniques," *Diagn. Interv. Imag.*, vol. 94, no. 5, pp. 487–495, May 2013, doi: 10.1016/j.diii.2013.01.022.

[15] J. Ormachea and K. J. Parker, "Elastography imaging: The 30 year perspective," *Phys. Med. Biol.*, vol. 65, no. 24, Dec. 2020, Art. no. 24TR06, doi: 10.1088/1361-6560/abca00.

[16] K. F. Graff, *Wave Motion in Elastic Solids*. New York, NY, USA: Dover Publications, 1991.

[17] K. J. Glaser et al., "Review of MR elastography applications and recent developments," *J. Magn. Reason. Imag.*, vol. 36, no. 4, pp. 757–774, Oct. 2012, doi: 10.1002/jmri.23597.

[18] J. Ormachea and K. J. Parker, "Reverberant shear wave phase gradients for elastography," *Phys. Med. Biol.*, vol. 66, no. 17, Aug. 2021, Art. no. 175001, doi: 10.1088/1361-6560/ac1b37.

[19] K. J. Parker et al., "Reverberant shear wave fields and estimation of tissue properties," *Phys. Med. Biol.*, vol. 62, no. 3, pp. 1046–1061, Jan. 2017, doi: 10.1088/1361-6560/aa5201.

[20] K. J. Parker and B. A. Maye, "Partially coherent radiation from reverberant chambers," *J. Acoust. Soc. Amer.*, vol. 76, no. 1, pp. 309–313, Jul. 1984, doi: 10.1121/1.391063.

[21] F. Zvietcovich et al., "Reverberant 3D optical coherence elastography maps the elasticity of individual corneal layers," *Nat. Commun.*, vol. 10, no. 1, Oct. 2019, Art. no. 4895, doi: 10.1038/s41467-019-12803-4.

[22] L. A. Aleman-Castañeda, F. Zvietcovich, and K. J. Parker, "Reverberant elastography for the elastic characterization of anisotropic tissues," *IEEE J. Sel. Top. Quantum Electron*, vol. 27, no. 4, Jul./Aug. 2021, Art. no. 7201312, doi: 10.1109/JSTQE.2021.3069098.

[23] H. Asemani et al., "Angular Integral autocorrelation for speed estimation in shear wave elastography," *Acoustics*, vol. 6, no. 2, pp. 413–438, May 2024, doi: 10.3390/acoustics6020023.

[24] H. Asemani et al., "Angular integration autocorrelation approach for shear wave speed estimation in the framework of reverberant shear wave elastography," in *Proc. 2024 IEEE UFFC Latin Amer. Ultrasonics Symp.*, 2024, pp. 1–3, doi: 10.1109/LAUS60931.2024.10553108.

[25] B. E. Treeby and B. T. Cox, "K-wave: Matlab toolbox for the simulation and reconstruction of photoacoustic wave fields," *J. Biomed. Opt.*, vol. 15, no. 2, Mar. 2010, Art. no. 021314, doi: 10.1117/1.3360308.

[26] T. Loupas, J. T. Powers, and R. W. Gill, "An axial velocity estimator for ultrasound blood flow imaging, based on a full evaluation of the doppler equation by means of a two-dimensional autocorrelation approach," *IEEE Trans. Ultrason. Ferroelectr. Freq. Control*, vol. 42, no. 4, pp. 672–688, Jul. 1995, doi: 10.1109/58.393110.

[27] J. Ormachea et al., "An initial study of complete 2D shear wave dispersion images using a reverberant shear wave field," *Phys. Med. Biol.*, vol. 64, Jul. 2019, Art. no. 145009, doi: 10.1088/1361-6560/ab2778.

[28] I. E. Kabir et al., "Reverberant magnetic resonance elastographic imaging using a single mechanical driver," *Phys. Med. Biol.*, vol. 68, no. 5, Feb. 2023, Art. no. 055015, doi: 10.1088/1361-6560/acbbb7.